PERSPECTIVES

Nanostructuring versus microstructuring in battery electrodes

Rishabh Jain, Aniruddha Singh Lakhnot, Kevin Bhimani, Shyam Sharma🆔,
Varad Mahajani, Reena A. Panchal🆔, Mithil Kamble, Fudong Han,
Chunsheng Wang🆔 and Nikhil Koratkar🆔

Abstract | Battery electrodes comprise a mixture of active material particles, conductive carbon and binder additives deposited onto a current collector. Although this basic design has persisted for decades, the desired size scale of the active material particle is a matter of debate. Advances in nanotechnology have spurred interest in deploying nanoparticles as the active material. In this Perspective, we compare the features of nanoparticle and microparticle electrodes, and discuss why the battery industry is unlikely to replace microstructures with nanometre-sized analogues. We then address the question of whether there is a place for nanomaterials in battery design. We suggest that the way forward lies in microscale particles with built-in nanoscale features, such as microparticles assembled from nanoscale building blocks or patterned with engineered or natural nanopores. These multiscale particles offer exciting possibilities to develop battery electrodes that are quintessentially both micro and nano with respect to their performance attributes.

Modern human society cannot flourish without an efficient, affordable and safe means of energy storage. Today, rechargeable lithium-ion batteries (LIBs) dominate the energy storage landscape from portable electronics to the rapidly expanding electric vehicle and electricity (grid) storage markets. The cost of LIBs is at present about US$150 kWh^{-1} but it is dropping; the US Department of Energy concludes that below a threshold of around US$100 kWh^{-1}, LIBs will be more cost-effective than an internal combustion engine vehicle[1–3]. As a result, electric vehicle sales, which already exceed a million units per year, are expected to see explosive growth to about 30 million units per year by 2030 (REFS.[1,4]). The grid energy storage sector is also predicted to grow rapidly over the next decade owing to increasing reliance on renewable but intermittent energy sources such as wind and solar[5]. Consequently, by 2030, global LIB demand is expected to soar to 1,200–1,600 GWh, roughly ten times the demand in 2020 (REF.[1]).

Although LIBs represent the best available rechargeable battery technology, a substantial gap in both energy and power density exists between LIBs and petrol[6]. There is thus considerable need for further improvement in LIB performance. The energy and power density of LIBs strongly depend on both the composition[7–13] and particle size[14,15] of the active electrode materials, the latter of which also affects the electrode fabrication process. Therefore, deploying active electrode materials with the desired particle size is an important design consideration for the battery engineer.

In the context of batteries, a nanostructured electrode contains active material particles in the size range 1–100 nm, whereas a microstructured electrode uses micrometre-sized (≥1 μm) particles. Over the past two decades, advances in nanotechnology have substantially improved nanostructured electrode performance[16,17]. Nanostructured electrodes offer clear advantages in terms of high rate capability, power density, higher lithium solubility and gravimetric capacity, reduced memory effect, as well as superior fracture toughness and fatigue resistance. Despite these advances, industry has so far resisted the mass

market adoption and direct (one-to-one) replacement of microstructured electrodes with their nanostructured counterparts. We analyse the underlying reasons for this, including their low first-cycle Coulombic efficiency, poor volumetric performance and low mass loading, and the high manufacturing cost and complexity associated with the use of nanoparticles, and conclude that nanostructured electrodes are unlikely to directly displace the incumbent microstructured electrode technology.

What then, if any, is the role of nanotechnology in battery development? We suggest that to achieve substantial improvement over state-of-the-art (microstructured) batteries, active material particles in future batteries must be inherently 'multiscale' in nature — microscale in size with in-built nanoscale features, thus reaping the benefits of both scales in the same system. How best to achieve these multiscale particles is an open question. Besides performance, manufacturing scale-up, safety and cost considerations are also important factors in determining whether such multiscale particle technologies can move forward into engineering practice.

In this Perspective, we compare nanostructured and microstructured electrodes and describe their advantages and disadvantages from the thermodynamic, kinetic and mechanical points of view. We review promising approaches towards achieving multiscale particles, including the self-assembly of nanometre-sized active materials into micrometre-sized particulates, and the use of microparticles with engineered or naturally occurring nanoporosity. We hope that this Perspective will help the academic and industrial battery communities to better contextualize the role of microstructuring and nanostructuring in battery design, and to accelerate the development of superior electrode architectures for future LIBs.

Nanostructuring versus microstructuring
Owing to the different size scales of the active material particles, nanostructured and microstructured electrodes exhibit different kinetic, thermodynamic and mechanical properties.

Kinetics. Fast-charging capability in high-energy-density LIBs is an important design requirement for electrification of automobiles. For an electrode with high tortuosity, solid-state diffusion of Li ions and electrons is usually the rate-limiting step, determining the rate capability of the battery[18]. Sufficient electronic conductivity in these electrodes is generally achieved by using conductive nanometre-sized carbon additives as an inactive component of the electrode, which speeds up electron conduction[19]. Therefore, we focus our discussion on Li$^+$ diffusion into the active material particle and on the relationship between particle size and the maximum achievable charge–discharge rate (C-rate) of the battery.

The diffusivity (D_i) of Li ions can be calculated using the Arrhenius equation: $D_i = D_o e(-\Delta G_m/KT)$, where D_o is a pre-factor determined empirically, k is the Boltzmann constant, T is the temperature and ΔG_m is the energy barrier for migration[18,20]. The time required (τ) for Li ions to diffuse into the active material particle (FIG. 1a) can be predicted using Einstein's formula: $\tau = \lambda^2/D_i$, where λ is the transverse length dependent on particle size[18,20]. Assuming D_i to be independent of particle size, the maximum achievable C-rate can be obtained using the relation: $C_D = 3,600 D_i/\lambda^2$, where C_D is the bulk-diffusion-limited C-rate[21]. Therefore, reducing λ about tenfold by switching from microparticles ($\lambda \approx 1\,\mu m$) to nanoparticles ($\lambda \approx 100\,nm$) can reduce τ and increase C_D by about 100-fold, enabling quick charging and discharging capability. Similarly, for alloying and conversion chemistries, the time taken for the reaction front to propagate through the particle and complete the phase transition is quicker in nanometre-sized than in micrometre-sized particles.

Therefore, nanostructured materials have been extensively studied, in order to fabricate LIBs with high-rate capability[22,23]. FIGURE 1b compares the rate performances of LIBs with nanoparticle and microparticle lithium titanium oxide ($Li_4Ti_5O_{12}$ (LTO)) electrodes[22,23]. At a rate of 1C, half cells assembled with lithium metal show a similar gravimetric capacity for both nanometre- and micrometre-sized LTO. However, when the current density is increased to 100C (that is, 36 seconds charging time), micrometre-sized LTO exhibits a negligible gravimetric capacity. By contrast, nanometre-sized LTO with an average particle size of 15–55 nm delivers approximately 70 mAh g^{-1} capacity at 100C, which further increases to 160–170 mAh g^{-1}

as particle size is reduced to 3–7 nm (REFS.[22,23]). The 3–7 nm LTO can even be operated at ultrafast rates of up to 400C (9 seconds charging time) while delivering about 72% of its theoretical capacity (FIG. 1b). Nanostructuring has a similar positive impact on high-rate capability for a broad range of intercalation, alloying and conversion-type electrode materials (TABLE 1). Thus, nanostructuring holds the key to developing LIBs with high power density, which is crucial to keep pace with the demands of customers for increasingly higher power and quicker charging.

D_i is generally independent of particle size. However, sphere-like particles that contain 1D migration channels can exhibit faster Li$^+$ diffusion when the particulates are nanometre-sized. For example, $LiFePO_4$, $LiMnBO_3$ and $LiFeSO_4F$ particles containing 1D migration channels are prone to antisite disorder defects, which originate during material synthesis[24–26]. Unlike in bulk materials, Li$^+$ diffusion through 1D channels is blocked by immobile or low-mobility defects in those channels[25]. For a fixed defect concentration, the probability of having two or more defects in a migration channel increases with channel length; the blocked areas between these defects make certain pathways inaccessible for Li$^+$ entering from either side of the channel[25,26] (FIG. 1c). The diffusion constant and specific capacity decrease when Li$^+$ ions are unable to circumvent the defects. Nanostructuring can mitigate the adverse effect of such defects on rate capability and specific capacity. Because nanometre-sized spherical particles have nanometre-scale channel lengths, they are less likely than microscale particles to carry two or more defects in a single migration channel — and thus they have very few or no blocked areas[25,26] (FIG. 1c). It should be noted that the above discussion pertains to 1D channels formed within sphere-like particles. 1D materials can also form fibre or rod-like particles with nanometre-scale diameter and micrometre-scale longitudinal dimensions[27]. In some cases, Li$^+$ diffusion is prohibited along the lateral dimension and can take place only along the micrometre-scale longitudinal direction[28,29]. In such cases, the adverse effect of defects on lithium diffusion will be prevalent even in 1D materials.

Thermodynamics. Microparticles of certain electrode materials (such as $LiFePO_4$ or TiO_2) exhibit a room-temperature miscibility gap wherein Li-poor and Li-rich phases coexist in a certain composition range ($0.05 < x < 0.89$ in the case of Li_xFePO_4)[30].

Outside of this composition range, either only the Li-poor phase ($Li_\alpha FePO_4$ where $0 < \alpha < 0.05$) or the Li-rich phase ($Li_\beta FePO_4$ where $0.89 < \beta < 1.0$) exists[30]. As the particle size is reduced from the micrometre- to the nanometre scale, the miscibility gap narrows (for ~40-nm Li_xFePO_4, the composition range is $0.12 < x < 0.83$)[30–32]. The coexistence of distinct phases in a nanoparticle is energetically less favourable than the existence of a single phase owing to lattice-mismatch-induced strain in the particle, which increases as the particle size is reduced[33–36]. Therefore, the phase separation energy gain decreases with nanostructuring, thus closing the miscibility gap[31] (FIG. 1d).

A reduced miscibility gap in smaller particles translates into increased solid solubility of lithium, which allows smaller particles to deliver higher reversible capacity[37] (FIG. 1e). For example, lithium solubility in the α phase of small ~7-nm TiO_2 particles (Li/Ti ~0.22) is much higher than that in bigger ~120-nm particles (Li/Ti ~0.03)[37]. Similarly, certain electrode materials deemed inactive in their bulk state, such as rutile TiO_2, perform adequately as LIB electrode materials after nanostructuring, owing to a decreased miscibility gap and higher solid solubility[38,39].

Nanostructuring can also affect the reaction voltage[40–44]. For microstructured electrodes, the excess energy generated through the surface ($3\Omega\sigma/r$, where σ is the surface free energy, r is the particle radius and Ω is the volume of the lithiated unit) is negligible[40]. However, when r is reduced to the nanometre scale, the free energy of the constituent phases increases significantly, which alters the chemical potential of the electrode and leads to a deviation in the voltage profile[40]. FIGURE 1f illustrates how a reduction in particle size modifies the voltage profile of $LiFePO_4$ (REF.[40]).

The memory effect in LIBs is also influenced by particle sizing. The memory effect describes the bump in voltage (or voltage overshoot) observed in the cycle following an incomplete charge–discharge cycle. It can result in incorrect estimation of the state-of-charge and adversely affect the capacity, durability and safety of the battery[45–48]. The effect has been reported in several materials that undergo phase transformation, such as $LiFePO_4$ and TiO_2, and is strongest in materials with delayed phase transitions. The memory effect and voltage overshoot is substantially reduced in nanoparticles, which have faster phase changes than their microscale counterparts[45] (FIG. 1g). Because it is

energetically unfavourable for two phases (such as Li-poor (α) and Li-rich (β) phases) to coexist in a nanoparticle[45,46], phase transitions occur rapidly in nanoparticles to release the excess free energy generated from lattice mismatch and high surface area. By contrast, in microparticles there is no substantial energy cost associated with phase separation, so phase transitions are relatively slow[46].

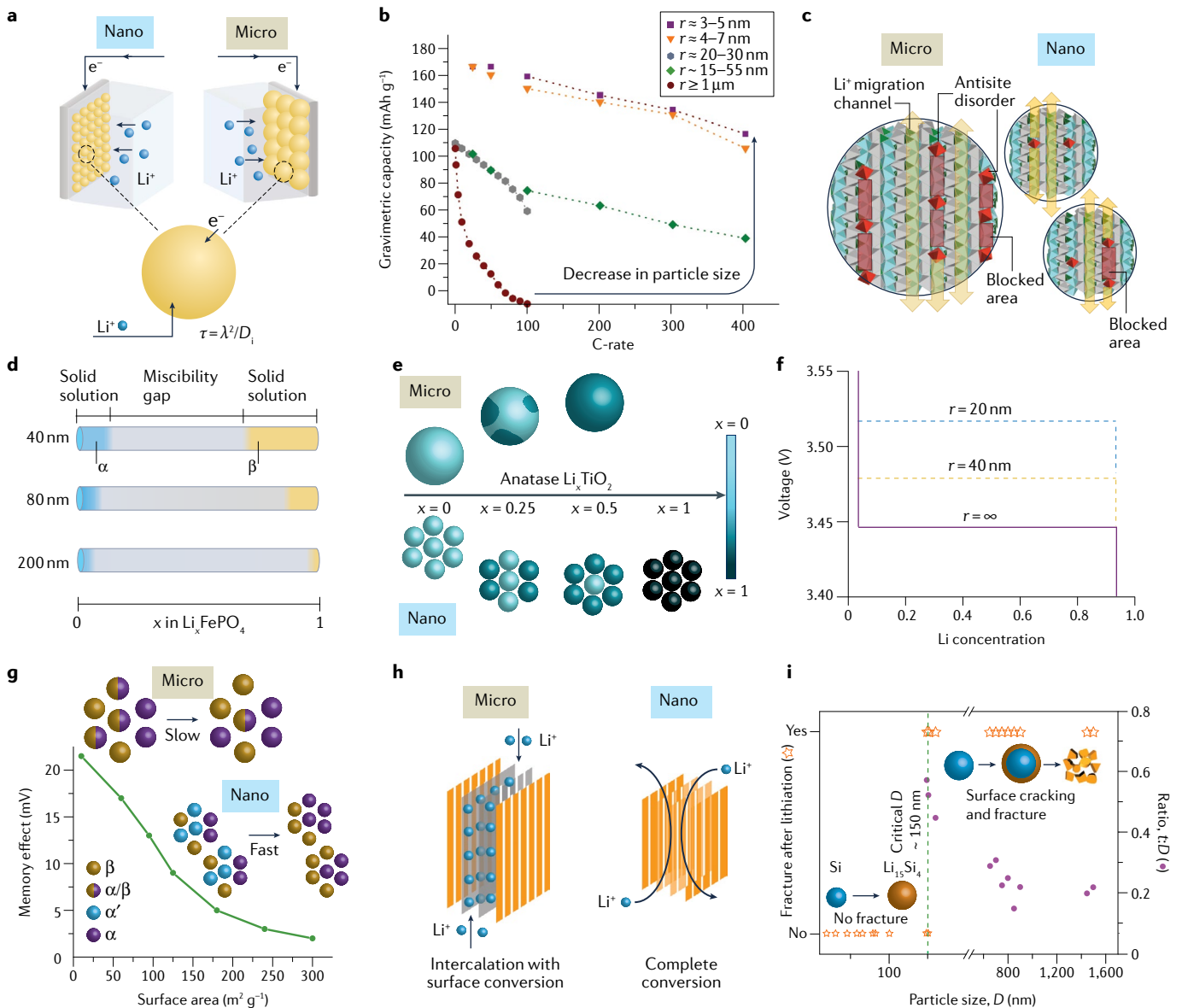The reaction pathway is also altered by nanostructuring, especially for

Fig. 1 | **Kinetic, thermodynamic and mechanical properties of nanometre- and micrometre-sized active material particles in Li-ion batteries. a** | Size-dependent diffusion of lithium ions (Li⁺) in the active material. The time required (τ) for Li⁺ to diffuse into the particle is directly proportional to the square of the transverse length (λ), which depends on particle size. D_i denotes the diffusivity of Li⁺ ions. **b** | Size-dependent gravimetric performance of $Li_4Ti_5O_{12}$ electrode at variable charge–discharge rates (C-rates) confirms that higher capacity at high C-rate can be achieved in nanometre-sized particles owing to their faster kinetics. **c** | Size-dependent impact of immobile antisite defect on Li⁺ transport in an electrode material with 1D ion channels. Owing to the smaller channel lengths in nanoparticles, the probability that antisite defects will block Li⁺ channels in nanoparticles is lower than for microparticles. **d** | Schematic illustration depicting decrease in miscibility gap in $LiFePO_4$ with decrease in particle size; x indicates lithiation extent in $FePO_4$. **e** | Schematic illustration depicting increase in solid solubility of lithium in TiO_2 electrodes with decrease in particle size; x indicates lithiation extent in TiO_2. **f** | Size-dependent voltage plateau in $LiFePO_4$; r is the active material size. **g** | Size-dependent memory effect in Li-ion batteries, showing lower impact of incomplete charging/discharging on battery performance while employing nanometre-sized active materials; α, α′ and β are different phases observed when the active material undergoes lithiation. **h** | Difference in reaction pathway in micrometre- and nanometre-sized $NbSe_3$. The nanometre-sized particle undergoes uniform lithiation, while the micrometre-sized particle undergoes stepwise lithiation. **i** | The size-dependent fracture mechanism in silicon anodes indicates the higher mechanical stability of nanoparticles than microparticles; D is the silicon particle diameter and t is the shell thickness of Li_xSi. Data in panel **b** adapted with permission from REF.[22], Wiley, and REF.[23], Elsevier. Panel **c** adapted with permission from REF.[26], Wiley. Panel **d** adapted with permission from REF.[31], Wiley. Panel **e** adapted with permission from REF.[37], copyright 2007 American Chemical Society. Panel **f** adapted with permission from REF.[40], Elsevier. Data in panel **g** adapted with permission from REF.[45], Wiley, and adapted with permission from REF.[46], copyright 2018 American Chemical Society. Panel **h** adapted with permission from REF.[52], copyright 2016 American Chemical Society. Panel **i** adapted with permission from REF.[59], copyright 2012 American Chemical Society.

Table 1 | **Performance of nanometre- and micrometre-sized cathode and anode materials explored for lithium-ion batteries**

Type	Electrode material	Particle size	Gravimetric capacity (mAh g^{-1})	Volumetric capacity (mAh l^{-1})	Cyclic stability (capacity retention)	C-rate (capacity retention)	First cycle Coulombic efficiency (%)
Cathode	LCO[112]	300 nm	203	≤690	93% (50 cycles)	49.7% (7C)	86
		1 µm	194	776–1,363[a]	63% (50 cycles)	10% (7C)	94
	LFP[113–115]	20–200 nm	130–169	90	–	80% (2C)	–
		0.4–6 µm	72–115	225	–	33% (2C)	≥97
	NCA[116,117]	200–500 nm	196	370	≥95% (100 cycles)	80% (1.37 A g^{-1})	70
		≥1 µm	170	420	78% (100 cycles)	75% (1.37 A g^{-1})	83.7
	LNMO[118]	80 nm	129	396	62% (500 cycles)	69% (11.8 A g^{-1})	83
		3–5 µm	108	407	95% (500 cycles)	46% (11.8 A g^{-1})	90
	FeF$_3$ (REF.[119])	30–50 nm	160	–	85% (100 cycles)	75.7% (1.2 A g^{-1})	84
		1–3 µm	106	–	60% (100 cycles)	35.5% (1.2 A g^{-1})	90
	LMFP[63]	≤100 nm	160	261.1	88.5% (50 cycles)	81% (2C)	87.5[a]
		7 µm	140	369.3	88% (50 cycles)	78% (2C)	93.5[a]
	C–S (REF.[120])	10 nm	1,600	–	87.5% (100 cycles)	55% (6.6 A g^{-1})	≤93[a]
		150 nm	1,000	–	80% (100 cycles)	22% (6.6 A/g^{-1})	≥95[a]
Anode	Si (REFS.[121,122])	5–100 nm	1,500–3,000	≤500	≥50% (10 cycles)	92% (2 A g^{-1})	65–80
		≥1 µm	500–1,500	1,200–1,500	≤9 % (10 cycles)	45% (2 A g^{-1})	≥90
	Fe$_2$O$_3$ (REFS.[49,123–125])	4–200 nm	800–1,000	950–1,200	80% (10 cycles)	70% (5 A g^{-1})	70–80
		0.5–5 µm	300–700	1,500–3,000	≤50% (10 cycles)	37% (5 A g^{-1})	≥95
	Nb$_2$O$_5$ (REFS.[97,126,127])	20–50 nm	75–160	50–80	71% (100 cycles)[a]	86% (20C)	85–95
		1 µm	175	190	78% (100 cycles)[a]	57% (20C)	95
	V$_2$O$_5$ (REFS.[128,129])	40–100 nm	140.3	64.54	79.4% (100 cycles)	82.5% (3 A g^{-1})	97.7
		3–6 µm	135	136.35	104% (60 cycles)	71% (2 A g^{-1})	98.5
	Co$_3$O$_4$ (REFS.[130,131])	70–100 nm	1,068[b]	587.4	97% (100 cycles)	77% (5 A g^{-1})	76
		4–8 µm	1,539[b]	3,231.9	28.4% (45 cycles)	–	74
	C (REFS.[132–134])	Nanosheets	567	≤300	65–100% (100 cycles)	54% (3.5 A g^{-1})	75.9
		Bulk	372	400–800	85% (100 cycles)	27% (3.5 A g^{-1})	84
	TiO$_2$ (REFS.[41,135–138])	≤100 nm	240–280	–	60% (20 cycles)	80% (5 A g^{-1})	80
		0.3–5 µm	≤200	–	45% (20 cycles)	60% (5 A g^{-1})	96

The table shows typical values taken from the literature[41,49,63,97,112–138]. All data are produced from lithium half-cell configurations. Retention values in the cycling stability column are at low C-rates. The number of cycles over which the retention is averaged is specified in the column. In the C-rate column, the maximum reported C-rate or operating current density is specified along with the capacity retention at that particular C-rate or current density. LCO, lithium cobalt oxide; LFP, lithium iron phosphate; LMFP, lithium manganese iron phosphate; LNMO, lithium nickel manganese oxide; NCA, lithium nickel cobalt aluminium oxide. [a]Ballpark measurement calculated either manually or predicted theoretically. [b]Capacity calculated at different current density.

conversion-based electrodes such as Fe$_2$O$_3$ and NbSe$_3$ (REFS.[49–53]). Lithiation in α-Fe$_2$O$_3$ can be described in three steps. In step 1, lithium intercalates, maintaining the original crystal structure; step 2 involves irreversible structural transformation to a cubic close-packed rock salt structure after the critical lithium concentration (X_c) has been reached; and in step 3 the close-packed structure converts to Li$_2$O and Fe^0. A direct comparison of nanometre- versus micrometre-sized α-Fe$_2$O$_3$ particles found that X_c is dependent on particle size: $X_c \approx 1$ for 20-nm particles and 0.03 for 0.5-µm particles[49]. Nanoparticles are able to lithiate uniformly owing to their small size. Micrometre-sized particles, being bigger, lithiate in stages (their outer surface first and then propagating to the core), undergo

non-homogeneous lithiation, and encounter higher structural stress, leading to early phase transformation. The differences in X_c affect the onset of step 3 (the conversion reaction): it starts early for microparticles, leading to the coexistence of multiple phases (α-Fe$_2$O$_3$, cubic Li$_2$Fe$_2$O$_3$, Fe^0 and Li$_2$O) and material inhomogeneity. For nanoparticles, step 3 is delayed, providing sufficient time for intercalation to complete. The reaction pathway in nanoparticles causes less stress compared to microparticles, which lends itself to better reversibility and cycle stability. It should, however, be noted that nanometre-sizing alone is not sufficient to guarantee long-term cycling stability. In addition to nanometre-sizing, composition optimization (such as binder and carbon additives)[54], electrode engineering

(3D architecture)[55], and chemical changes (such as fluorination)[56,57] are needed to boost cyclic stability.

The relationship between size and reaction pathway is also illustrated in NbSe$_3$ (REF.[52]). For NbSe$_3$ nanoribbons (diameter < 50 nm) the entire nanoribbon undergoes conversion, whereas the conversion reaction of bigger ribbons (~300 nm) is limited to the outer surface (FIG. 1h). There are a few reasons for this phenomenon. The conversion reaction is catalysed predominantly at surface defect sites. Given their lower surface-to-volume ratio, bigger particles lack such nucleation sites, which impedes the conversion process. Moreover, as the conversion reaction proceeds from the surface towards the bulk, it transmits high stress owing to

non-uniform volume changes within the particle. This impedes the propagation of the reaction, limiting it to the surface for larger ribbons[52]. As a result, nanometre-sized $NbSe_3$ can deliver a higher specific capacity than can micrometre-sized $NbSe_3$.

Mechanical stability. Nanostructuring provides improved mechanical stability over microstructuring, especially for alloying materials (such as silicon, phosphorus, aluminium, tin, antimony or bismuth) that undergo large volume changes during lithium insertion and extraction[20,58]. For example, in the case of silicon, in situ transmission electron microscopy has shown that below a critical diameter of ~150 nm ± 10 nm (FIG. 1i), silicon particles are resistant to stress-induced cracking and pulverization[59]. The stress build-up in silicon particles is related to a lithium concentration gradient at the interface, which results in a strain mismatch within the particle. The cracking of the microparticle relieves this stress. However, in the case of nanoparticles, when the particle diameter is of the order of or below the typical crack size, this effect is suppressed and the particle survives the lithiation/de-lithiation event[59]. Moreover, nanoparticles tend to lithiate more uniformly than microparticles, which also helps to mitigate strain mismatch and particle cracking. As a consequence, nanoparticles of alloying materials display far superior fracture toughness and fatigue life in the electrochemical environment of a LIB.

Why the industry prefers microparticles

Despite the fact that nanoparticles offer vastly superior high-rate capability and power density, extended Li-ion solubility, higher gravimetric capacity, reduced memory effect, and superior fracture and fatigue resistance, the LIB industry has yet to adopt nanoparticles as a direct replacement to microparticles. While there has been industrial activity directed at creating composite electrodes comprising both nanoparticles and microparticles, microparticles still remain the active material of choice in commercial LIBs. We offer our perspective as to why this has been the case.

Reduced Coulombic efficiency. The small size and ultrahigh specific surface area of nanoparticles is a double-edged sword. On the one hand, these features facilitate fast diffusion and high-rate performance. On the other, electrolyte decomposition over nanoparticle surfaces is responsible

for generating a massive amount of solid–electrolyte interface (SEI) in the first (formation) cycle of the battery[60]. This SEI drastically reduces the first-cycle Coulombic efficiency of the battery[61,62] (FIG. 2a).

The very large contact area between the nanoparticle and electrolyte also promotes side reactions and higher irreversibility in subsequent cycles. In a LIB full cell, a limitless supply of lithium is not available. Consequently, a low first-cycle Coulombic efficiency or relatively poor Coulombic efficiency in subsequent cycles will severely reduce the battery's cycle life. The electrolyte is also limited, and its constant decomposition will dry up the battery. These limitations are unacceptable to the industry, which is pushing for longer cycle and calendar life in applications such as electrification of automobiles and electricity (grid) storage.

Poor volumetric energy density. Although academic studies have tended to focus on gravimetric energy density (Wh kg⁻¹), the volumetric energy density (Wh l⁻¹) is far more relevant as a performance parameter for energy storage in compact spaces, where packing the maximum amount of energy into a limited volume becomes critical. For example, battery packs for electric vehicles, stationary (grid) storage and even portable electronics are volume- rather than weight-limited. The packing (or tap) density of nanoparticle-based electrodes tends to be poor owing to the presence of void space between the nanoparticles[63]. This void space has no impact on the gravimetric performance, but it greatly reduces the volumetric capacity and energy density of nanometre-sized compared to micrometre-sized materials[63] (FIG. 2b). Although repeated calendaring (that is, pressure-induced compaction) cycles have been used to improve the packing density of nanoparticle electrodes, their volumetric performance still falls well short of industrial standards[64].

Low mass loading and aggregation. To deliver longer battery life, the industry is aiming to maximize the mass loading of the electrode. At present, the industrial standard for electrode mass loading lies in the range 20–30 mg cm⁻². Achieving such high mass loadings at a reasonable electrode thickness (that is, a few tens of micrometres) is very challenging with nanoparticles owing to their relatively low tap density. Uncontrolled aggregation of nanoparticles also leads to deterioration in performance and poor reliability[65,66].

High cost and complexity. Nanoparticle electrodes are not easy to manufacture at large scale[67]. Nanostructuring generally requires arduous, time-consuming and expensive syntheses that produce a large amount of chemical waste, a major environmental concern[20,68,69]. Given their high surface area, nanomaterials are prone to oxidation, and so most of the synthetic steps must be performed in an inert environment, which is not cost-effective[29]. Furthermore, size homogeneity is difficult to achieve through nanostructuring and typically requires additional post-processing[29]. All of these steps increase the production cost and complexity of nanostructured electrodes compared with their microstructured counterparts.

Current industrial scenario

Although many industries have benefited from the advent of LIBs, the impact on the automobile industry has been truly transformative. The battery electric vehicle (BEV) market is in exponential growth mode and could completely displace combustion engine vehicles in the coming decade[70–76]. Several electrical vehicles were introduced in the past decade with improvement in gravimetric energy density (from ~120 to ~260 Wh kg⁻¹), volumetric energy density (from ~200 to ~680 Wh l⁻¹), and driving range (from ~120 to ~570 km)[70,75] (FIG. 2c). In spite of substantial gains in BEV performance, much improvement is still needed before BEVs can gain widespread community acceptance. For example, the average time to refuel a petrol vehicle is less than 5 minutes, whereas the best-performing Tesla cars still take about 15 minutes at a supercharging station to allow a driving range of around 320 kilometres. FIGURE 2d illustrates current estimates and aspirational BEV battery targets up to the year 2030 (REFS.[71,77]). Volumetric and gravimetric energy density require a fourfold to fivefold improvement between now and 2030 in order to displace petrol-powered vehicles. BEVs must become considerably cheaper to fabricate and safer for passengers to use. They must also generate much greater power over a wide temperature range. Lastly, faster charging is mandatory for BEVs to compete with petrol vehicles and gain community acceptance.

Microscale particles with nanoscale attributes

Continued BEV improvement is contingent on our ability to improve the structure and function of active material particles used in battery electrodes. FIGURE 2e and TABLE 1 compare the performance

of nanometre- and micrometre-sized electrode materials with the same composition undergoing different types of electrochemical reactions. Nanometre-sized particles outperform their micrometre-sized counterparts in terms of gravimetric capacity, charging rate and cycle retention but perform less well in volumetric capacity and first-cycle Coulombic efficiency. Neither nanoparticles nor microparticles can meet the BEV performance, cost and safety targets indicated in FIG. 2d. What, then,

is the way forward? In our view, the next generation of active material particles deployed in future battery systems must be inherently multiscale in nature — that is, they must be micrometre-sized, yet endowed with nanoscale features or attributes — in order to keep pace with the demand for ever-improving batteries. In other words, the attractive features of both nanoparticles and microparticles must be combined in a single multiscale particle to get the best of both worlds. In the following sections, we review

some promising approaches to accomplish this outcome.

Engineered nanoporosity. To boost the performance of LIBs, high-capacity alloying anodes are being considered as an alternative to intercalation anodes. Alloying materials, such as silicon, typically suffer from poor cycle life owing to pulverization and cracking during the lithiation/delithiation process[78–80]. Stress build-up during lithiation/delithiation can be
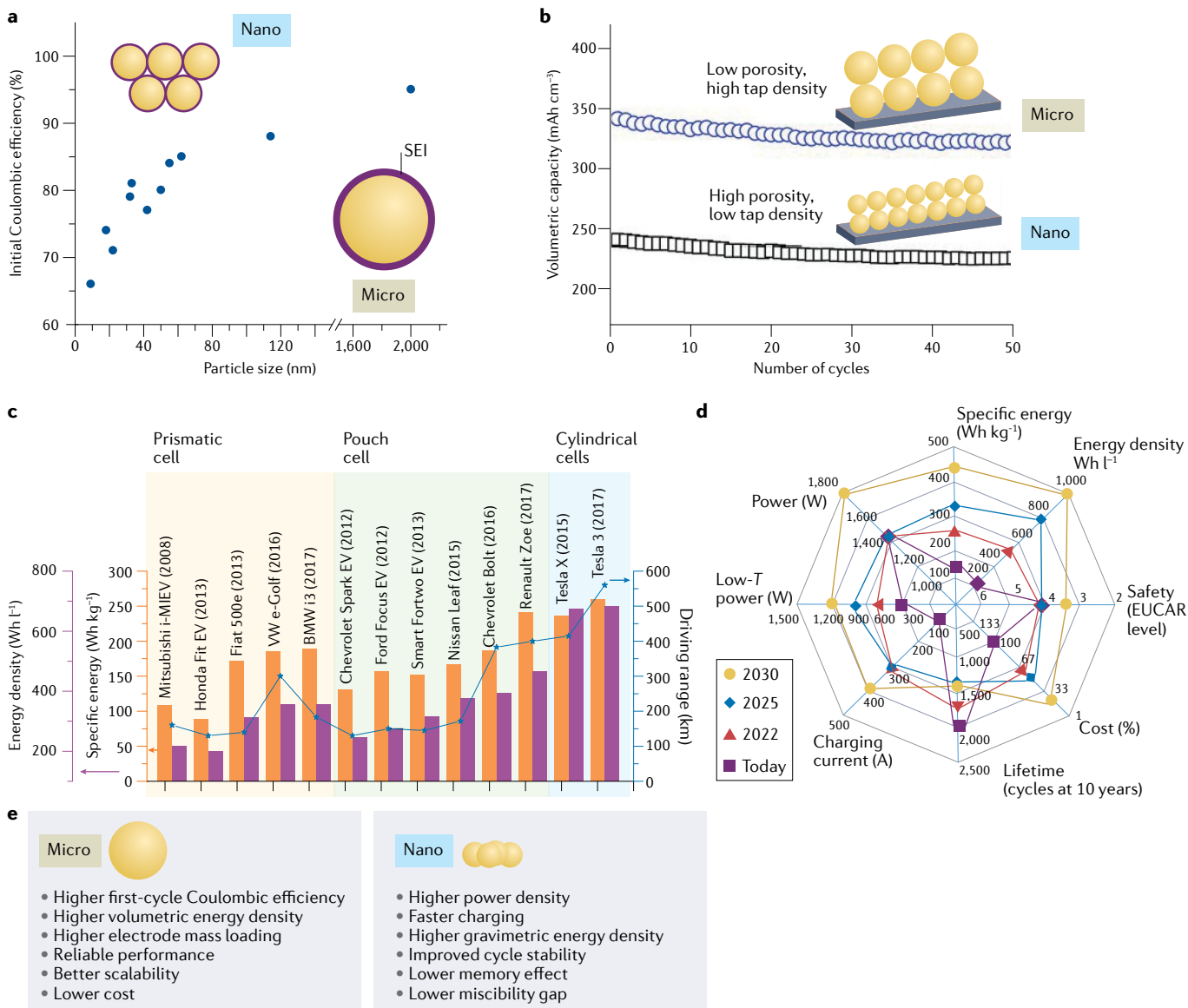

Fig. 2 | **Shortcomings of nanostructuring and current industrial scenario for battery-electric vehicles. a** | Particle-size-dependent first-cycle Coulombic efficiencies for lithium-ion batteries with silicon anodes. Owing to a higher ratio of surface area to volume, which leads to greater decomposition of the electrolyte, the first-cycle Coulombic efficiency of nanoparticles is lower than for microparticles. **b** | Volumetric capacity comparison of nanometre- and micrometre-sized $LiMn_{0.85}Fe_{0.15}PO_4$ (LMFP) at 0.05C. Owing to higher packing density and lower empty (void) space, micrometre-sized particles exhibit superior volumetric capacity, when compared to nanometre-sized particles. **c** | Energy density, specific energy and driving range of various battery electric vehicles currently on the market. **d** | Road map for key performance parameters at the cell level for fully electrified vehicles from today up to the year 2030. **e** | Schematic depicting the advantages of microparticles and nanoparticles in lithium-ion battery applications. Data in panel **a** adapted from REF.[61], CC BY 4.0 (https://creativecommons.org/licenses/by/4.0/). Panel **b** adapted with permission from REF.[63], Wiley. Data in panel **c** adapted from REF.[75], Springer Nature Limited. Data in panel **d** adapted with permission from REF.[71], Royal Society of Chemistry, and obtained from REF.[77].
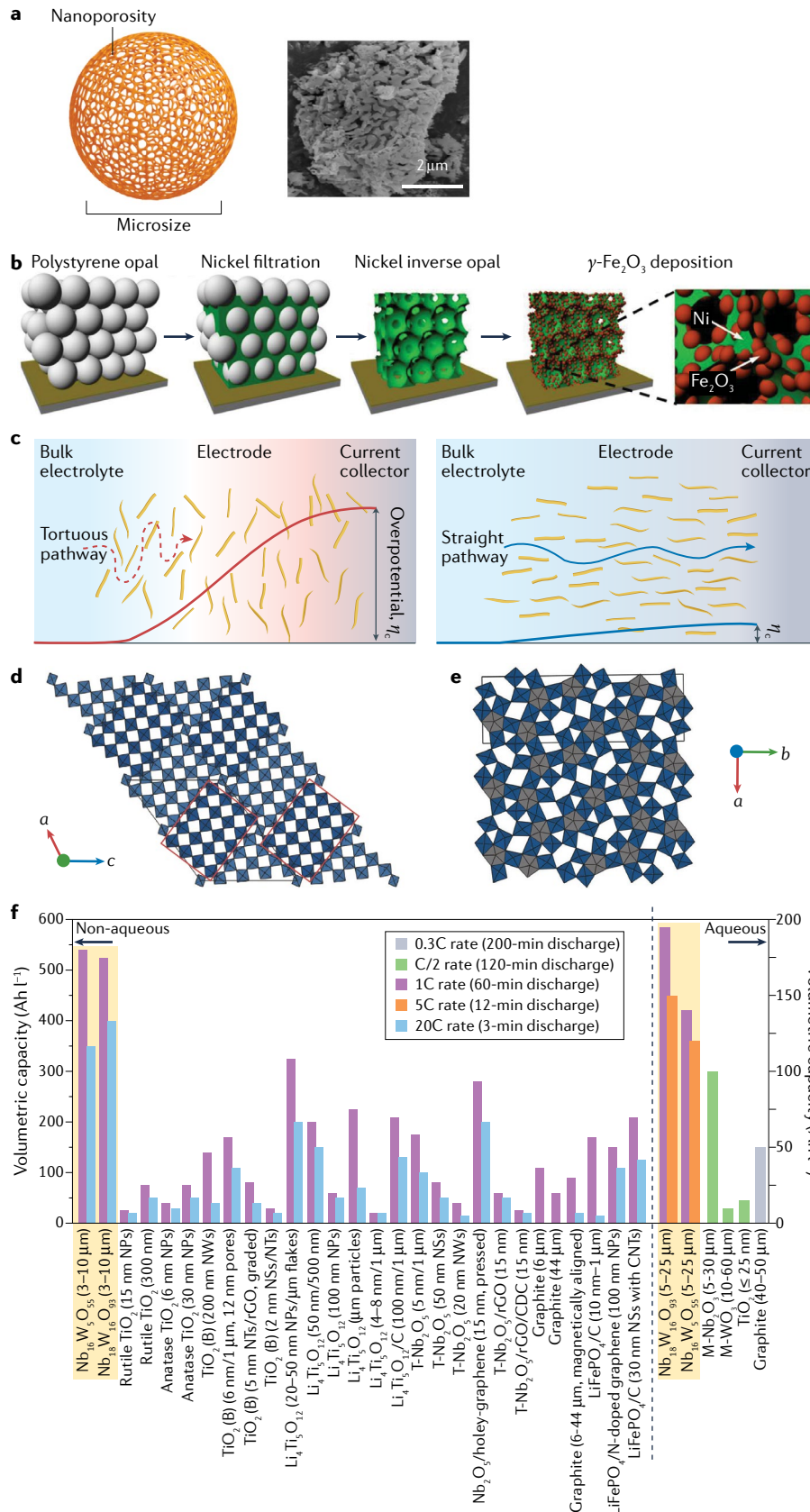
a Nanoporosity

Microsize

b Polystyrene opal — Nickel filtration — Nickel inverse opal — γ-Fe₂O₃ deposition

Ni
Fe₂O₃

c

Bulk electrolyte | Electrode | Current collector

Tortuous pathway

Overpotential, η_c

Bulk electrolyte | Electrode | Current collector

Straight pathway

η_c

d

a
c

e

b
a

f

Non-aqueous — Aqueous

Fig. 3 | **Microparticles with engineered or natural nanoporosity. a** | Schematic illustration (left) and SEM micrograph (right) showing ant-nest-like micrometre-sized silicon with engineered nanoporosity. The particle undergoes cycling without pulverization, cracking or delamination. **b** | Mesoporous and continuous 3D nickel current collector substrate decorated with γ-Fe₂O₃ nanoparticles (NPs). The manufacturing process involves self-assembly of polystyrene opal microparticles. Nickel inverse opal structure is obtained by electrodepositing nickel through the polystyrene opal structure and then treating it with toluene or tetrahydrofuran to remove the polystyrene spheres. Finally, NPs of the active material (γ-Fe₂O₃) are loaded onto the nickel inverse opal structure by pulse voltage deposition. **c** | Alignment of particles with a layered structure in the thickness direction of the electrode. Left schematic shows unaligned particles and thus a tortuous pathway, whereas right schematic shows that aligning particles reduces tortuosity to provide a straighter pathway for direct lithium transport. **d,e** | Natural nanoporosity is observed in certain classes of materials, such as niobium tungsten oxides. The crystal structure in panel **d** is $Nb_{16}W_5O_{55}$, constructed through blocks (red rectangles) of 4×5 (Nb,W)O₆ octahedra connected at corners (parallelogram with black lines indicates the unit cell) and, in panel **e**, a $Nb_{18}W_{16}O_{93}$ superstructure is shown, made up of tetragonal tungsten bronze (blue) with pentagonal tunnels (grey) partially filled by –W–O chains that form pentagonal bipyramids (the rectangle with black lines indicates the unit cell). **f** | Volumetric capacity comparison of $Nb_{16}W_5O_{55}$ and $Nb_{18}W_{16}O_{93}$ in non-aqueous and aqueous lithium-ion batteries with other often-used electrode data taken from the literature. CDC, carbide derived carbon; CNT, carbon nanotube; NS, nanosheet; NT, nanotube; NW, nanowire; rGO, reduced graphene oxide. Panel **a** reprinted from REF.[84], CC BY 4.0 (https://creativecommons.org/licenses/by/4.0/). Panel **b** reprinted with permission from REF.[92], American Chemical Society. Panel **c** reprinted from REF.[96], Springer Nature Limited. Panels **d** and **e** reprinted from REF.[97], Springer Nature Limited. Data in panel **f** reprinted from REF.[97], Springer Nature Limited, and adapted with permission from REF.[101], Elsevier.

LIBs, but are limited by complex and costly synthesis[83].

In one method, porous Si microparticles were fabricated through nitridation of Mg–Si alloy, followed by removal of Mg₃N₂ byproducts[84]. The resulting 'ant-nest-like' microparticles had an average diameter of $3 \pm 0.2\,\mu m$ and contained a multitude of ~50-nm nanopores (FIG. 3a). Nanopores provide buffer space for the Si microparticles to expand and contract during lithiation and delithiation, leading to high structural stability and stable electrochemical performance[84]. Engineering of nanopores

mitigated by engineering nanometre-sized pores in micrometre-sized alloy-based particles. Several synthesis techniques can create these porous microparticles, including

metal deposition and chemical etching, as well as assembly of nanometre-sized building blocks[81,82]. These strategies lead to stable cycling of silicon microparticles in

into microparticles has also been utilized to overcome pulverization and cracking in other alloying materials such as red phosphorus[85]. Porosity can be engineered by various approaches such as hollowing of materials[86], solid-state decomposition[87], hard/soft templating[88], microemulsion templating[81,89] and template-free synthesis[90,91].

The best features of both microparticles and nanoparticles can also be captured by depositing nanoparticles of the active material on a continuous 3D mesoporous scaffold. This strategy has been reported for γ-Fe_2O_3 particles on a nickel scaffold[92] (FIG. 3b). The mesostructured architecture, being highly porous, accommodates volume expansion and contraction during charge–discharge cycles, and ensures that the electrolyte has better accessibility to the active material. Additionally, the nickel current collector serves as an efficient pathway for electron conduction. This multiscale electrode delivered reversible capacities of ~1,000 mAh g^{-1} and ~450 mAh g^{-1} at 0.2C and 20C, respectively. Voltage hysteresis was low compared to the non-multiscale Fe_2O_3 literature[93,94], and the particle size of the cycled electrodes remained stable at ~20 nm.

Porosity can be engineered not only at the particle level, but also at the electrode level[95]. For example, sheet-like microparticles can be aligned in the direction of electrode thickness to create less tortuous pathways for direct lithium transport (FIG. 3c). Such alignment can be engineered using numerous approaches[96]. In one method, application of an external magnetic field during electrode synthesis aligns the particles[95].

Natural nanoporosity. Certain micrometre-scale materials are naturally endowed with nanoscale channels or tunnels that are capable of fast Li$^+$ transport. One such class of materials are complex oxides such as niobium tungsten oxides, like $Nb_{16}W_5O_{55}$ and $Nb_{18}W_{16}O_{93}$. $Nb_{16}W_5O_{55}$ belongs to the Wadsley–Roth type of crystallographic shear structure and is composed of blocks of (4 × 5) MO_6 (M = Nb, W) octahedra[97] (FIG. 3d). The octahedra inside the blocks are corner-shared, forming tetragonal channels. These (4 × 5) block subunits are connected by crystallographic shear planes at the edges, and four such subunits are connected by a WO_4 tetrahedron at the corner. $Nb_{18}W_{16}O_{93}$ has a pseudo-tetragonal tungsten bronze structure[97] consisting of NbO_6 and WO_6 octahedra, which form pentagonal, tetragonal and triangular tunnels (FIG. 3e).

Some of the pentagonal tunnels are occupied by W–O chains and are edge-shared with the neighbouring octahedra, which form twisted locked octahedra and frustrated polyhedral networks. In both $Nb_{16}W_5O_{55}$ and $Nb_{18}W_{16}O_{93}$, the ubiquitous tunnels and channels enable ultrafast diffusion of Li ions. Further, substantial edge-sharing prevents structural rearrangement, and therefore maintains high Li$^+$ mobility through the channels[97]. This behaviour is in stark contrast to simple oxides (such as ReO_3) that are prone to structural phase transition during lithiation, negatively affecting lithium mobility[98]. These characteristics enable niobium tungsten oxides to achieve ultrafast operation at charge–discharge rates of up to 100C, which is unprecedented in traditional microparticle-based electrodes. The presence of open tunnels also provides buffer space for volume expansion, which mitigates stress-induced fracture. In addition, these oxides possess multiple redox couples (Nb^{4+}/Nb^{5+}, Nb^{3+}/Nb^{4+}, W^{5+}/W^{6+} and W^{4+}/W^{5+}) active at safe potentials above 1 V (versus Li/Li$^+$)[97]. Because all of these redox reactions occur above 1 V, this material is unlikely to encounter lithium plating during fast charging, which is a major safety concern for low-voltage anodes such as graphite[99] and silicon[100]. There is, however, a trade-off: high-potential anodes lower the battery voltage, which reduces energy density.

Volumetrically, the performances of $Nb_{16}W_5O_{55}$ and $Nb_{18}W_{16}O_{93}$ are some of the best reported to date. In non-aqueous electrolytes, these niobium tungsten oxides delivered higher capacity at low rates (520–530 Ah l^{-1} at 1C) and at high rates (350–400 Ah l^{-1} at 20C) in comparison with conventional electrode materials[97] (FIG. 3f). Similarly, with aqueous electrolytes, the oxides delivered stable volumetric capacities of 124–200 Ah l^{-1} at 1C and 117–148 Ah l^{-1} at 5C, which substantially outperformed all other reported materials in aqueous batteries[101] (FIG. 3f). Although the volumetric energy and power density of these oxide materials are stellar, the same cannot be said of their gravimetric numbers, owing to the presence of heavy elements such as Nb and W. The discovery of new oxide compositions with lighter and/or cheaper elements — such as the Wadsley–Roth-derived layered niobates $NaNb_3O_8$ and KNb_3O_8 synthesized last year[102] — may considerably improve gravimetric performance and cost effectiveness. Facile Li transport pathways may also extend beyond complex oxide phases to include other classes of metal oxides. For example, fast Li-ion transport

routes in lithium titanate ($Li_4Ti_5O_{12}$) arise from intermediate configurations involving face-shared Li polyhedra[103].

Assembly of nanoscale constituents. High-energy-conversion cathodes are also being explored as an alternative to intercalation-based LIBs. Conversion cathodes based on materials such as sulfur exhibit very low electronic conductivity, which makes it challenging to deploy them as microparticles. Multiscale particles, in which nanometre-sized carbon–sulfur (C–S) primary particles are assembled into micrometre-sized secondary particles, can solve this problem (FIG. 4a). To achieve this, sulfur can be melt-diffused into the matrix of a microscale carbon cluster (diameter ~1–2 μm) that is composed of many smaller hollow carbon nanospheres (diameter ~120 nm)[104]. The resulting C–S cluster is coated with a polymer, poly(3,4-ethylenedioxythiopene) (PEDOT), to buffer the volume expansion of sulfur and to prevent polysulfide shuttle (FIG. 4b). A Li–S battery with a PEDOT-C–S cluster-based electrode delivered high gravimetric capacity (~1,000 mAh g^{-1}) and rate capability (up to 3C), with excellent Coulombic efficiency (>99.5 %). Importantly, owing to its high tap density, the PEDOT-C–S also delivered high volumetric performance (~1,290 Wh l^{-1} at 3C).

Multiscale particles can also be formed by the dense molecular-level mixing of S and C into nanometre-sized composite particles, and their subsequent aggregation into larger microscale secondary particles[105] (FIG. 4c,d). Sulfur was decomposed in the presence of oxygen and a nitrogen-rich carbon source, leading to small sulfur molecules (S_2 and S_3) chemically bonded with carbon (C–S and O–S bonds), forming a dense nanometre-sized carbon–sulfur (C–S) composite, which then aggregates into microparticles. Given its molecularly dense nature with the presence of nanometre-sized primary particles, the C–S electrode displayed superior rate capability (~322 mAh g^{-1} at ~32 A g^{-1} current density). In addition, solid-state reactions between small S molecules and Li ($4Li^+ + SO + 4e^- \leftrightarrow Li_2S + Li_2O$) prevent the formation of liquid lithium polysulfides, which are responsible for capacity fade in conventional Li–S batteries[105]. Consequently, the C–S composite was able to deliver high specific capacity (~836 mAh g^{-1} at ~500 mA g^{-1} current density) with high capacity retention (~0.025% capacity decay per cycle) and very high Coulombic efficiency (~100%) over
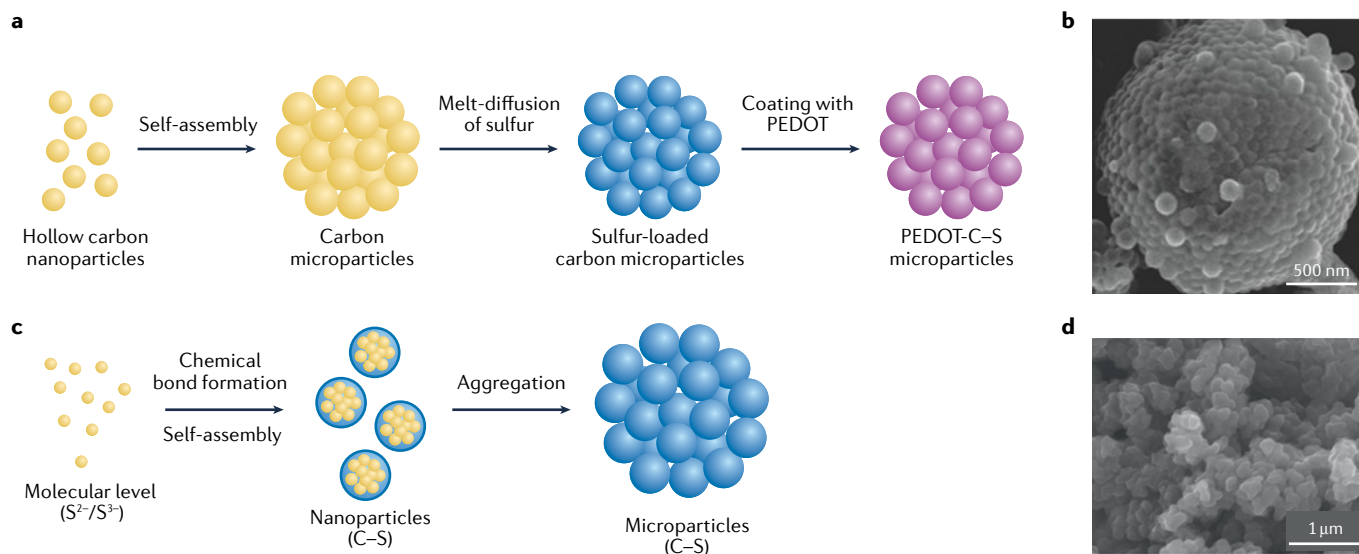
Fig. 4 | **Microscale particles assembled using nanoscale building blocks for high-energy conversion cathodes. a** | Schematic depicting the self-assembly of hollow carbon nanospheres into microscale carbon clusters, which are then impregnated with sulfur, forming carbon–sulfur (C–S) microparticles. In the final step, the C–S microparticles are coated with layer of the conductive polymer poly(3,4-ethylenedioxythiopene) (PEDOT). The purpose of the carbon is to improve electronic conductivity, while the polymer also provides conductivity, buffers the volume expansion of sulfur and suppresses polysulfide shuttle. **b** | Scanning electron microscopy (SEM) image of a typical PEDOT-C–S multiscale particle. **c** | Schematic depicting molecular sulfur confined into nanometre-sized particles with carbon coating. These particles subsequently aggregate into larger microscale particles. **d** | SEM image of the multiscale C–S particles. Panel **b** reprinted with permission from REF.[104], Wiley. Panel **d** reprinted with permission from REF.[105], National Academy of Sciences.

1,000 charge–discharge steps[105]. Multiscale nano- and micro-architectures have also been used to create composites of Chevrel-phase Mo_6S_8 and sulfur for Li–S batteries[106].

Concluding remarks

The size scale of the active material particles used in the anode and cathode has a crucial role in LIB performance. In this Perspective, we show through thermodynamic, kinetic and mechanical analyses that nanoparticles offer clear advantages over microparticles in terms of fast-charging capability, superior power density, higher solid solubility and gravimetric capacity, reduced memory effect and superior cycle life. Yet the industry continues to favour microparticles in commercial battery products. We suggest that the industry's reluctance to adopt nanoparticles stems from their low first-cycle Coulombic efficiency, poor tap density and volumetric performance, low mass loading, complex manufacturing processes and increased cost of use. These general conclusions apply to both anode and cathode materials.

Although microparticle- and nanoparticle-based electrodes have unique sets of pros and cons, in our judgement, the issue of micro versus nano is a false choice. If we are to significantly outperform today's LIB technology, future active material particles will need to realize the best performance attributes of both the micrometre and nanometre scales.

Multiscale particles that feature densely packed or molecularly mixed nanoscale constituents in a microscale package show great promise for improved cathodes in conversion-based LIB and lithium–sulfur chemistries. Similarly, anode microparticles with engineered nanoporosity enable relatively stable cycling of alloying anodes, because the presence of free volume within the bulk microparticles provides stress relief. Nanoporosity need not always be engineered; it also occurs naturally in certain classes of materials, such as complex oxides of niobium and tungsten, whose microscale structures are endowed with built-in nanoscale channels and tunnels for fast Li^{+} intercalation. These complex oxides may have a transformative impact on the high rate (or equivalently high power density) performance of LIBs, enabling LIBs perhaps to rival the performance of supercapacitors, without compromising on volumetric performance, mass loading or first-cycle Coulombic efficiency. The drawback of niobium tungsten oxides is that they contain heavy and expensive elements, which negatively affects their gravimetric performance and cost attributes. Future efforts should aim to discover alternate oxide chemistries that feature lighter and/or cheaper elements.

In general, our comparisons of nanoparticles versus microparticles hold for solid electrolytes in addition to liquid electrolytes. Limitations in the electrochemical stability window[107] can cause decomposition of solid electrolytes, especially in high-voltage solid-state batteries. Because solid electrolytes are immobile, the SEI formed in solid-state batteries is not as dynamic (that is, it is frozen at the solid-state interface) as that in liquid-electrolyte-based batteries[108]. Reformation of the SEI is commonly observed in liquid-electrolyte batteries, arising from cracking/pulverization of active materials[109]. Such effects are suppressed in solid electrolytes owing to the frozen SEI, which explains why micrometre-sized silicon anodes show poor cycle stability in liquid-electrolyte batteries, but can work well in solid-state batteries[110]. The formation of a purely inorganic SEI in solid-state batteries also mitigates the challenges associated with high-capacity electrodes. It is worth mentioning that the properties, especially the ionic and electronic conductivities, of the SEI formed in solid-state batteries are highly dependent on the composition of the solid electrolyte. For solid electrolytes that form electronically conductive interphases, it is not advisable to use nanometre-sized (that is, high-surface-area) and electronically conductive active materials, owing to increased electronic conductivity of the solid electrolyte[111].

While the abovementioned technologies could have a breakthrough impact from an electrochemical performance perspective, it

should be emphasized that manufacturing, scaling up, safety and cost considerations will have the ultimate say in establishing commercial viability. That being said, active material particles that are multiscale in nature — microscale in size but with nanoscale attributes — are likely to be ubiquitous in future batteries.

Rishabh Jain[1], Aniruddha Singh Lakhnot[1], Kevin Bhimani[1], Shyam Sharma ⬛[1], Varad Mahajani[2], Reena A. Panchal ⬛[1], Mithil Kamble[1], Fudong Han[1], Chunsheng Wang ⬛[3]✉ and Nikhil Koratkar ⬛[1,2]✉

[1]Department of Mechanical, Aerospace and Nuclear Engineering, Rensselaer Polytechnic Institute, Troy, NY, USA.

[2]Department of Materials Science and Engineering, Rensselaer Polytechnic Institute, Troy, NY, USA.

[3]Department of Chemical and Biomolecular Engineering, University of Maryland, College Park, MD, USA.

✉e-mail: cswang@umd.edu; koratn@rpi.edu

1. Goldman, A. R., Rotondo, F. S. & Swallow, J. G. Lithium ion battery industrial base in the US and abroad (Institute for Defense Analyses, 2019).
2. Nykvist, B. & Nilsson, M. Rapidly falling costs of battery packs for electric vehicles. *Nat. Clim. Chang.* **5**, 329–332 (2015).
3. Ziegler, M. S. & Trancik, J. E. Re-examining rates of lithium-ion battery technology improvement and cost decline. *Energy Environ. Sci.* **14**, 1635–1651 (2021).
4. Lutsey, N. & Nicholas, M. Update on electric vehicle costs in the United States through 2030 (International Council on Clean Transportation, 2019).
5. Gür, T. M. Review of electrical energy storage technologies, materials and systems: challenges and prospects for large-scale grid storage. *Energy Environ. Sci.* **11**, 2696–2767 (2018).
6. Hundekar, P., Jain, R., Lakhnot, A. S. & Koratkar, N. Recent advances in the mitigation of dendrites in lithium-metal batteries. *J. Appl. Phys.* **128**, 10903 (2020).
7. Ellis, B. L., Lee, K. T. & Nazar, L. F. Positive electrode materials for Li-ion and Li-batteries. *Chem. Mater.* **22**, 691–714 (2010).
8. Lotfabad, E. M. et al. High-density sodium and lithium ion battery anodes from banana peels. *ACS Nano* **8**, 7115–7129 (2014).
9. Liu, C., Li, F., Ma, L.-P. & Cheng, H.-M. Advanced materials for energy storage. *Adv. Mater.* **22**, E28–E62 (2010).
10. Naguib, M. et al. New two-dimensional niobium and vanadium carbides as promising materials for Li-ion batteries. *J. Am. Chem. Soc.* **135**, 15966–15969 (2013).
11. Whittingham, M. S. Materials challenges facing electrical energy storage. *MRS Bull.* **33**, 411–419 (2008).
12. Dang, J. et al. Synthesis and electrochemical performance characterization of Ce-doped $Li_3V_2(PO_4)_3$/C as cathodes for lithium-ion batteries. *J. Power Sources* **243**, 33–39 (2013).
13. Obrovac, M. N. & Chevrier, V. L. Alloy negative electrodes for Li-ion batteries. *Chem. Rev.* **114**, 11444–11502 (2014).
14. Lu, J. et al. The role of nanotechnology in the development of battery materials for electric vehicles. *Nat. Nanotechnol.* **11**, 1031–1038 (2016).
15. Aricò, A. S., Bruce, P., Scrosati, B., Tarascon, J.-M. & van Schalkwijk, W. Nanostructured materials for advanced energy conversion and storage devices. *Nat. Mater.* **4**, 366–377 (2005).
16. Mukherjee, R., Krishnan, R., Lu, T.-M. & Koratkar, N. Nanostructured electrodes for high-power lithium ion batteries. *Nano Energy* **1**, 518–533 (2012).
17. Sun, Y., Liu, N. & Cui, Y. Promises and challenges of nanomaterials for lithium-based rechargeable batteries. *Nat. Energy* **1**, 16071 (2016).
18. Tang, Y., Zhang, Y., Li, W., Ma, B. & Chen, X. Rational material design for ultrafast rechargeable lithium-ion batteries. *Chem. Soc. Rev.* **44**, 5926–5940 (2015).
19. Jain, R. et al. Reversible alloying of phosphorene with potassium and its stabilization using reduced graphene oxide buffer layers. *ACS Nano* **13**, 14094–14106 (2019).
20. Qi, W. et al. Nanostructured anode materials for lithium-ion batteries: principle, recent progress and future perspectives. *J. Mater. Chem. A* **5**, 19521–19540 (2017).
21. Tsai, P.-C. et al. Single-particle measurements of electrochemical kinetics in NMC and NCA cathodes for Li-ion batteries. *Energy Environ. Sci.* **11**, 860–871 (2018).
22. Feckl, J. M., Fominykh, K., Döblinger, M., Fattakhova-Rohlfing, D. & Bein, T. Nanoscale porous framework of lithium titanate for ultrafast lithium insertion. *Angew. Chem. Int. Ed.* **51**, 7459–7463 (2012).
23. Bresser, D. et al. The importance of "going nano" for high power battery materials. *J. Power Sources* **219**, 217–222 (2012).
24. Seo, D.-H. et al. Intrinsic nanodomains in triplite $LiFeSO_4F$ and its implication in lithium-ion diffusion. *Adv. Energy Mater.* **8**, 1701408 (2018).
25. Malik, R., Burch, D., Bazant, M. & Ceder, G. Particle size dependence of the ionic diffusivity. *Nano Lett.* **10**, 4123–4127 (2010).
26. Kim, J. C., Seo, D.-H., Chen, H. & Ceder, G. The effect of antisite disorder and particle size on Li intercalation kinetics in monoclinic $LiMnBO_3$. *Adv. Energy Mater.* **5**, 1401916 (2015).
27. Housel, L. M. et al. Investigation of α-MnO_2 tunneled structures as model cation hosts for energy storage. *Acc. Chem. Res.* **51**, 575–582 (2018).
28. Ekaterina, P., Francesco, B., Xinliang, F., Yi, C. & Yury, G. Energy storage: the future enabled by nanomaterials. *Science* **366**, 6468 (2019).
29. Jung, S.-K. et al. Nanoscale phenomena in lithium-ion batteries. *Chem. Rev.* **120**, 6684–6737 (2020).
30. Yamada, A. et al. Room-temperature miscibility gap in Li_xFePO_4. *Nat. Mater.* **5**, 357–360 (2006).
31. Kobayashi, G. et al. Isolation of solid solution phases in size-controlled Li_xFePO_4 at room temperature. *Adv. Funct. Mater.* **19**, 395–403 (2009).
32. Meethong, N., Huang, H.-Y. S., Carter, W. C. & Chiang, Y.-M. Size-dependent lithium miscibility gap in nanoscale $Li_{1-x}FePO_4$. *Electrochem. Solid State Lett.* **10**, A134 (2007).
33. Meethong, N., Huang, H.-Y. S., Speakman, S. A., Carter, W. C. & Chiang, Y.-M. Strain accommodation during phase transformations in olivine-based cathodes as a materials selection criterion for high-power rechargeable batteries. *Adv. Funct. Mater.* **17**, 1115–1123 (2007).
34. Wagemaker, M., Mulder, F. M. & Van der Ven, A. The role of surface and interface energy on phase stability of nanosized insertion compounds. *Adv. Mater.* **21**, 2703–2709 (2009).
35. Burch, D. & Bazant, M. Z. Size-dependent spinodal and miscibility gaps for intercalation in nanoparticles. *Nano Lett.* **9**, 3795–3800 (2009).
36. Wagemaker, M. et al. Dynamic solubility limits in nanosized olivine $LiFePO_4$. *J. Am. Chem. Soc.* **133**, 10222–10228 (2011).
37. Wagemaker, M., Borghols, W. J. H. & Mulder, F. M. Large impact of particle size on insertion reactions. a case for anatase Li_xTiO_2. *J. Am. Chem. Soc.* **129**, 4323–4327 (2007).
38. Borghols, W. J. H., Wagemaker, M., Lafont, U., Kelder, E. M. & Mulder, F. M. Impact of nanosizing on lithiated rutile TiO_2. *Chem. Mater.* **20**, 2949–2955 (2008).
39. Hu, Y.-S., Kienle, L., Guo, Y.-G. & Maier, J. High lithium electroactivity of nanometer-sized rutile TiO_2. *Adv. Mater.* **18**, 1421–1426 (2006).
40. Van der Ven, A. & Wagemaker, M. Effect of surface energies and nano-particle size distribution on open circuit voltage of Li-electrodes. *Electrochem. Commun.* **11**, 881–884 (2009).
41. Kang, W. et al. Particle size effect of anatase TiO_2 nanocrystals for lithium-ion batteries. *J. Electrochem. Soc.* **158**, A59 (2011).
42. Liu, P., Vajo, J. J., Wang, J. S., Li, W. & Liu, J. Thermodynamics and kinetics of the Li/FeF_3 reaction by electrochemical analysis. *J. Phys. Chem. C* **116**, 6467–6473 (2012).
43. Okubo, M. et al. Nanosize effect on high-rate Li-ion intercalation in $LiCoO_2$ electrode. *J. Am. Chem. Soc.* **129**, 7444–7452 (2007).
44. Lee, K. T., Kan, W. H. & Nazar, L. F. Proof of intercrystallite ionic transport in $LiMPO_4$ electrodes (M = Fe, Mn). *J. Am. Chem. Soc.* **131**, 6044–6045 (2009).
45. Madej, E., La Mantia, F., Schuhmann, W. & Ventosa, E. Impact of the specific surface area on the memory effect in Li-ion batteries: the case of anatase TiO_2. *Adv. Energy Mater.* **4**, 1400829 (2014).
46. Guo, X. et al. Size-dependent memory effect of the $LiFePO_4$ electrode in Li-ion batteries. *ACS Appl. Mater. Interfaces* **10**, 41407–41414 (2018).
47. Sasaki, T., Ukyo, Y. & Novák, P. Memory effect in a lithium-ion battery. *Nat. Mater.* **12**, 569–575 (2013).
48. Jia, J., Tan, C., Liu, M., Li, D. & Chen, Y. Relaxation-induced memory effect of $LiFePO_4$ electrodes in Li-ion batteries. *ACS Appl. Mater. Interfaces* **9**, 24561–24567 (2017).
49. Larcher, D. et al. Effect of particle size on lithium intercalation into α-Fe_2O_3. *J. Electrochem. Soc.* **150**, A133 (2003).
50. Bock, D. C. et al. Size dependent behavior of Fe_3O_4 crystals during electrochemical (de)lithiation: an in situ X-ray diffraction, ex situ X-ray absorption spectroscopy, transmission electron microscopy and theoretical investigation. *Phys. Chem. Chem. Phys.* **19**, 20867–20880 (2017).
51. Menard, M. C., Takeuchi, K. J., Marschilok, A. C. & Takeuchi, E. S. Electrochemical discharge of nanocrystalline magnetite: structure analysis using X-ray diffraction and X-ray absorption spectroscopy. *Phys. Chem. Chem. Phys.* **15**, 18539–18548 (2013).
52. Luo, L., Zhao, B., Xiang, B. & Wang, C.-M. Size-controlled intercalation-to-conversion transition in lithiation of transition-metal chalcogenides — $NbSe_3$. *ACS Nano* **10**, 1249–1255 (2016).
53. Li, W. et al. Operando bulk and interfacial characterization for electrochemical energy storage: case study employing isothermal microcalorimetry and X-ray absorption spectroscopy. *J. Mater. Res.* **37**, 319–333 (2022).
54. Cabana, J., Monconduit, L., Larcher, D. & Palacín, M. R. Beyond intercalation-based Li-ion batteries: the state of the art and challenges of electrode materials reacting through conversion reactions. *Adv. Mater.* **22**, E170–E192 (2010).
55. Martha, S. K. et al. Electrode architectures for high capacity multivalent conversion compounds: iron (II and III) fluoride. *RSC Adv.* **4**, 6730–6737 (2014).
56. Zhou, H. et al. Controlled formation of mixed nanoscale domains of high capacity Fe_2O_3–FeF_3 conversion compounds by direct fluorination. *ACS Nano* **9**, 2530–2539 (2015).
57. Chevrier, V. L., Hautier, G., Ong, S. P., Doe, R. E. & Ceder, G. First-principles study of iron oxyfluorides and lithiation of FeOF. *Phys. Rev. B* **87**, 094118 (2013).
58. Graetz, J., Ahn, C. C., Yazami, R. & Fultz, B. Highly reversible lithium storage in nanostructured silicon. *Electrochem. Solid State Lett.* **6**, A194 (2003).
59. Liu, X. H. et al. Size-dependent fracture of silicon nanoparticles during lithiation. *ACS Nano* **6**, 1522–1531 (2012).
60. Xu, K. Electrolytes and interphases in Li-ion batteries and beyond. *Chem. Rev.* **114**, 11503–11618 (2014).
61. Keller, C. et al. Effect of size and shape on electrochemical performance of nano-silicon-based lithium battery. *Nanomaterials* **11**, 307 (2021).
62. Lai, S. Y. et al. Silicon nanoparticle ensembles for lithium-ion batteries elucidated by small-angle neutron scattering. *ACS Appl. Energy Mater.* **2**, 3220–3227 (2019).
63. Sun, Y.-K., Oh, S.-M., Park, H.-K. & Scrosati, B. Micrometer-sized, nanoporous, high-volumetric-capacity $LiMn_{0.85}Fe_{0.15}PO_4$ cathode material for rechargeable lithium-ion batteries. *Adv. Mater.* **23**, 5050–5054 (2011).
64. Karkar, Z. et al. How silicon electrodes can be calendered without altering their mechanical strength and cycle life. *J. Power Sources* **371**, 136–147 (2017).
65. Wang, F. et al. Conversion reaction mechanisms in lithium ion batteries: study of the binary metal fluoride electrodes. *J. Am. Chem. Soc.* **133**, 18828–18836 (2011).
66. Courtney, I. A., McKinnon, W. R. & Dahn, J. R. On the aggregation of tin in SnO composite glasses caused by the reversible reaction with lithium. *J. Electrochem. Soc.* **146**, 59–68 (1999).
67. Berckmans, G. et al. Cost projection of state of the art lithium-ion batteries for electric vehicles up to 2030. *Energies* **10**, 1314 (2017).
68. Fan, X. et al. Pomegranate-structured conversion-reaction cathode with a built-in Li source for high-energy Li-ion batteries. *ACS Nano* **10**, 5567–5577 (2016).
69. Hsu, K.-F., Tsay, S.-Y. & Hwang, B.-J. Synthesis and characterization of nano-sized $LiFePO_4$ cathode materials prepared by a citric acid-based sol–gel route. *J. Mater. Chem.* **14**, 2690–2695 (2004).

70. Blomgren, G. E. The development and future of lithium ion batteries. *J. Electrochem. Soc.* **164**, A5019–A5025 (2016).

71. Andre, D. et al. Future generations of cathode materials: an automotive industry perspective. *J. Mater. Chem. A* **3**, 6709–6732 (2015).

72. Kwade, A. et al. Current status and challenges for automotive battery production technologies. *Nat. Energy* **3**, 290–300 (2018).

73. Cao, Y., Li, M., Lu, J., Liu, J. & Amine, K. Bridging the academic and industrial metrics for next-generation practical batteries. *Nat. Nanotechnol.* **14**, 200–207 (2019).

74. Ue, M., Sakaushi, K. & Uosaki, K. Basic knowledge in battery research bridging the gap between academia and industry. *Mater. Horiz.* **7**, 1937–1954 (2020).

75. Schmuch, R., Wagner, R., Hörpel, G., Placke, T. & Winter, M. Performance and cost of materials for lithium-based rechargeable automotive batteries. *Nat. Energy* **3**, 267–278 (2018).

76. Masias, A., Marcicki, J. & Paxton, W. A. Opportunities and challenges of lithium ion batteries in automotive applications. *ACS Energy Lett.* **6**, 621–630 (2021).

77. European Council for Automotive R&D. Battery requirements for future automotive applications (EUCAR, 2019).

78. Lee, W. J. et al. N-doped graphitic self-encapsulation for high performance silicon anodes in lithium-ion batteries. *Energy Environ. Sci.* **7**, 621–626 (2014).

79. Jangid, M. K. & Mukhopadhyay, A. Real-time monitoring of stress development during electrochemical cycling of electrode materials for Li-ion batteries: overview and perspectives. *J. Mater. Chem. A* **7**, 23679–23726 (2019).

80. Gowda, S. R. et al. Three-dimensionally engineered porous silicon electrodes for Li ion batteries. *Nano Lett.* **12**, 6060–6065 (2012).

81. Liu, N. et al. A pomegranate-inspired nanoscale design for large-volume-change lithium battery anodes. *Nat. Nanotechnol.* **9**, 187–192 (2014).

82. Bang, B. M., Lee, J.-I., Kim, H., Cho, J. & Park, S. High-performance macroporous bulk silicon anodes synthesized by template-free chemical etching. *Adv. Energy Mater.* **2**, 878–883 (2012).

83. Magasinski, A. et al. High-performance lithium-ion anodes using a hierarchical bottom-up approach. *Nat. Mater.* **9**, 353–358 (2010).

84. An, W. et al. Scalable synthesis of ant-nest-like bulk porous silicon for high-performance lithium-ion battery anodes. *Nat. Commun.* **10**, 1447 (2019).

85. Zhu, J. et al. Green, template-less synthesis of honeycomb-like porous micron-sized red phosphorus for high-performance lithium storage. *ACS Nano* **15**, 1880–1892 (2021).

86. Lou, X. W. D., Archer, L. A. & Yang, Z. Hollow micro-/nanostructures: synthesis and applications. *Adv. Mater.* **20**, 3987–4019 (2008).

87. Xu, Y. et al. Controllable synthesis of 3D Fe_3O_4 micro-cubes as anode materials for lithium ion batteries. *CrystEngComm* **21**, 5050–5058 (2019).

88. He, H., Fu, C., An, Y., Feng, J. & Xiao, J. Biofunctional hollow γ-MnO_2 microspheres by a one-pot collagen-templated biomineralization route and their applications in lithium batteries. *RSC Adv.* **11**, 37040–37048 (2021).

89. Zhang, G. et al. Formation of $ZnMn_2O_4$ ball-in-ball hollow microspheres as a high-performance anode for lithium-ion batteries. *Adv. Mater.* **24**, 4609–4613 (2012).

90. Pan, A., Wu, H. B., Yu, L. & Lou, X. W. D. Template-free synthesis of VO_2 hollow microspheres with various interiors and their conversion into V_2O_5 for lithium-ion batteries. *Angew. Chem. Int. Ed.* **52**, 2226–2230 (2013).

91. Partheeban, T. & Sasidharan, M. Template-free synthesis of LiV_3O_8 hollow microspheres as positive electrode for Li-ion batteries. *J. Mater. Sci.* **55**, 2155–2165 (2020).

92. Wang, J., Zhou, H., Nanda, J. & Braun, P. V. Three-dimensionally mesostructured Fe_2O_3 electrodes with good rate performance and reduced voltage hysteresis. *Chem. Mater.* **27**, 2803–2811 (2015).

93. Reddy, M. V. et al. α-Fe_2O_3 nanoflakes as an anode material for Li-ion batteries. *Adv. Funct. Mater.* **17**, 2792–2799 (2007).

94. Wang, Z., Luan, D., Madhavi, S., Hu, Y. & Lou, X. W. Assembling carbon-coated α-Fe_2O_3 hollow nanohorns on the CNT backbone for superior lithium storage capability. *Energy Environ. Sci.* **5**, 5252–5256 (2012).

95. Billaud, J., Bouville, F., Magrini, T., Villevieille, C. & Studart, A. R. Magnetically aligned graphite electrodes for high-rate performance Li-ion batteries. *Nat. Energy* **1**, 16097 (2016).

96. Ju, Z., Zhang, X., Wu, J. & Yu, G. Vertically aligned two-dimensional materials-based thick electrodes for scalable energy storage systems. *Nano Res.* **14**, 3562–3575 (2021).

97. Griffith, K. J., Wiaderek, K. M., Cibin, G., Marbella, L. E. & Grey, C. P. Niobium tungsten oxides for high-rate lithium-ion energy storage. *Nature* **559**, 556–563 (2018).

98. Cava, R. J., Santoro, A., Murphy, D. W., Zahurak, S. M. & Roth, R. S. The structures of the lithium inserted metal oxides $Li_{0.2}ReO_3$ and $Li_{0.36}WO_3$. *J. Solid State Chem.* **50**, 121–128 (1983).

99. Downie, L. E. et al. In situ detection of lithium plating on graphite electrodes by electrochemical calorimetry. *J. Electrochem. Soc.* **160**, A588–A594 (2013).

100. Chae, S., Ko, M., Kim, K., Ahn, K. & Cho, J. Confronting issues of the practical implementation of Si anode in high-energy lithium-ion batteries. *Joule* **1**, 47–60 (2017).

101. Lakhnot, A. S. et al. Aqueous lithium-ion batteries with niobium tungsten oxide anodes for superior volumetric and rate capability. *Energy Stor. Mater.* **27**, 506–513 (2020).

102. McColl, K. et al. Energy storage mechanisms in vacancy-ordered Wadsley–Roth layered niobates. *J. Mater. Chem. A* **9**, 20006–20023 (2021).

103. Zhang, W. et al. Kinetic pathways of ionic transport in fast-charging lithium titanate. *Science* **367**, 1030–1034 (2020).

104. Li, W. et al. A sulfur cathode with pomegranate-like cluster structure. *Adv. Energy Mater.* **5**, 1500211 (2015).

105. Luo, C. et al. A chemically stabilized sulfur cathode for lean electrolyte lithium sulfur batteries. *Proc. Natl Acad. Sci. USA* **117**, 14712 (2020).

106. Xue, W. et al. Intercalation-conversion hybrid cathodes enabling Li–S full-cell architectures with jointly superior gravimetric and volumetric energy densities. *Nat. Energy* **4**, 374–382 (2019).

107. Han, F., Zhu, Y., He, X., Mo, Y. & Wang, C. Electrochemical stability of $Li_{10}GeP_2S_{12}$ and $Li_7La_3Zr_2O_{12}$ solid electrolytes. *Adv. Energy Mater.* **6**, 1501590 (2016).

108. Luntz, A. C., Voss, J. & Reuter, K. Interfacial challenges in solid-state Li ion batteries. *J. Phys. Chem. Lett.* **6**, 4599–4604 (2015).

109. Chen, J. et al. Electrolyte design for LiF-rich solid–electrolyte interfaces to enable high-performance microsized alloy anodes for batteries. *Nat. Energy* **5**, 386–397 (2020).

110. Tan, D. H. S. et al. Carbon-free high-loading silicon anodes enabled by sulfide solid electrolytes. *Science* **373**, 1494–1499 (2021).

111. Zhang, W. et al. The detrimental effects of carbon additives in $Li_{10}GeP_2S_{12}$-based solid-state batteries. *ACS Appl. Mater. Interfaces* **9**, 35888–35896 (2017).

112. Jo, M., Hong, Y.-S., Choo, J. & Cho, J. Effect of $LiCoO_2$ cathode nanoparticle size on high rate performance for Li-ion batteries. *J. Electrochem. Soc.* **156**, A430 (2009).

113. Liu, J., Wang, Z., Zhang, G., Liu, Y. & Yu, A. Size-controlled synthesis of $LiFePO_4$/C composites as cathode materials for lithium ion batteries. *Int. J. Electrochem. Sci.* **8**, 2378–2387 (2013).

114. Fey, G. T.-K., Chen, Y. G. & Kao, H.-M. Electrochemical properties of $LiFePO_4$ prepared via ball-milling. *J. Power Sources* **189**, 169–178 (2009).

115. Oh, S. W. et al. Nanoporous structured $LiFePO_4$ with spherical microscale particles having high volumetric capacity for lithium batteries. *Electrochem. Solid State Lett.* **12**, A181 (2009).

116. Xiao, P., Lv, T., Chen, X. & Chang, C. $LiNi_{0.8}Co_{0.15}Al_{0.05}O_2$: enhanced electrochemical performance from reduced cationic disordering in Li slab. *Sci. Rep.* **7**, 1408 (2017).

117. Yiğitalp, A., Taşdemir, A., Alkan Gürsel, S. & Yürüm, A. Nafion-coated $LiNi_{0.80}Co_{0.15}Al_{0.05}O_2$ (NCA) cathode preparation and its influence on the Li-ion battery cycle performance. *Energy Storage* **2**, e154 (2020).

118. Liu, H. et al. Morphological evolution of high-voltage spinel $LiNi_{0.5}Mn_{1.5}O_4$ cathode materials for lithium-ion batteries: the critical effects of surface orientations and particle size. *ACS Appl. Mater. Interfaces* **8**, 4661–4675 (2016).

119. Tan, J. et al. Iron fluoride with excellent cycle performance synthesized by solvothermal method as cathodes for lithium ion batteries. *J. Power Sources* **251**, 75–84 (2014).

120. Chen, H. et al. Monodispersed sulfur nanoparticles for lithium–sulfur batteries with theoretical performance. *Nano Lett.* **15**, 798–802 (2015).

121. Li, H. A high capacity nano-Si composite anode material for lithium rechargeable batteries. *Electrochem. Solid State Lett.* **2**, 547 (1999).

122. Zhu, G., Chao, D., Xu, W., Wu, M. & Zhang, H. Microscale silicon-based anodes: fundamental understanding and industrial prospects for practical high-energy lithium-ion batteries. *ACS Nano* **15**, 15567–15593 (2021).

123. Sun, M. et al. Porous Fe_2O_3 nanotubes as advanced anode for high performance lithium ion batteries. *Ceram. Int.* **43**, 363–367 (2017).

124. Lin, Y.-M., Abel, P. R., Heller, A. & Mullins, C. B. α-Fe_2O_3 nanorods as anode material for lithium ion batteries. *J. Phys. Chem. Lett.* **2**, 2885–2891 (2011).

125. Cho, J. S., Hong, Y. J., Lee, J.-H. & Kang, Y. C. Design and synthesis of micron-sized spherical aggregates composed of hollow Fe_2O_3 nanospheres for use in lithium-ion batteries. *Nanoscale* **7**, 8361–8367 (2015).

126. Liu, S. et al. Nb_2O_5 microstructures: a high-performance anode for lithium ion batteries. *Nanotechnology* **27**, 46LT01 (2016).

127. Liu, M., Yan, C. & Zhang, Y. Fabrication of Nb_2O_5 nanosheets for high-rate lithium ion storage applications. *Sci. Rep.* **5**, 8326 (2015).

128. Zhang, C., Chen, Z., Guo, Z. & Lou, X. W. D. Additive-free synthesis of 3D porous V_2O_5 hierarchical microspheres with enhanced lithium storage properties. *Energy Environ. Sci.* **6**, 974–978 (2013).

129. An, Q. et al. Three-dimensional porous V_2O_5 hierarchical octahedrons with adjustable pore architectures for long-life lithium batteries. *Nano Res.* **8**, 481–490 (2015).

130. Yuan, W. et al. Preparation of porous Co_3O_4 polyhedral architectures and its application as anode material in lithium-ion battery. *Mater. Lett.* **97**, 129–132 (2013).

131. Zhan, L., Wang, S., Ding, L.-X., Li, Z. & Wang, H. Grass-like Co_3O_4 nanowire arrays anode with high rate capability and excellent cycling stability for lithium-ion batteries. *Electrochim. Acta* **135**, 35–41 (2014).

132. Mukherjee, R. et al. Defect-induced plating of lithium metal within porous graphene networks. *Nat. Commun.* **5**, 3710 (2014).

133. Liu, C. et al. Nitrogen-doped graphene by all-solidstate ball-milling graphite with urea as a high-power lithium ion battery anode. *J. Power Sources* **342**, 157–164 (2017).

134. Lin, P.-C., Wu, J.-Y. & Liu, W.-R. Green and facile synthesis of few-layer graphene via liquid exfoliation process for lithium-ion batteries. *Sci. Rep.* **8**, 9766 (2018).

135. Jiang, C. et al. Particle size dependence of the lithium storage capability and high rate performance of nanocrystalline anatase TiO_2 electrode. *J. Power Sources* **166**, 239–243 (2007).

136. Saito, M. et al. Improvement of the reversible capacity of TiO_2(B) high potential negative electrode. *J. Electrochem. Soc.* **159**, A49–A54 (2011).

137. Jiang, C., Honma, I., Kudo, T. & Zhou, H. Nanocrystalline rutile TiO_2 electrode for high-capacity and high-rate lithium storage. *Electrochem. Solid State Lett.* **10**, A127 (2007).

138. Ren, Y. et al. Nanoparticulate TiO_2(B): an anode for lithium-ion batteries. *Angew. Chem. Int. Ed.* **51**, 2164–2167 (2012).

Author contributions
R.J., C.W. and N.K. envisioned and developed the Perspective. R.J., A.S.L., K.B., S.S., V.M., R.A.P., M.K. and N.K. carried out the literature survey, analysed the data and prepared the figures. R.J., A.S.L., K.B., F.H., C.W. and N.K. wrote the Perspective.

Competing interests
The authors declare no competing interests.

Peer review information
Nature Reviews Materials thanks Kaifu Huo and the other, anonymous, reviewer(s) for their contribution to the peer review of this work.

Publisher's note
Springer Nature remains neutral with regard to jurisdictional claims in published maps and institutional affiliations.